Supplementary Information

A Multi-Sensor-Integrated Organs-on-Chips Platform for Automated and Continual *in situ* Monitoring of Organoid Behaviors

Yu Shrike Zhang[a,b,c,†,*], **Julio Aleman**[a,b,d,†], **Su Ryon Shin**[a,b,c,†], **Tugba Kilic**[a,b,e], **Duckjin Kim**[a,b], **Seyed Ali Mousavi Shaegh**[a,b,f], **Solange Massa**[a,b,g], **Reza Riahi**[a,b], **Sukyoung Chae**[a,b], **Ning Hu**[a,b,h], **Huseyin Avci**[a,b,i], **Weijia Zhang**[a,b,j], **Antonia Silvestri**[a,b,k], **Amir Sanati Nazhad**[a,b,l], **Ahmad Manbohi**[a,b,m], **Fabio De Ferrari**[a,b,k], **Alessandro Polini**[a,b], **Giovanni Calzone**[a,b], **Noor Shaikh**[a,b,n], **Parissa Alerasool**[a,b], **Erica Budina**[a,b], **Jian Kang**[a,b], **Nupura Bhise**[a,b], **João Ribas**[a,b,o], **Adel Pourmand**[a,b,p], **Aleksander Skardal**[d], **Thomas Shupe**[d], **Colin Bishop**[d], **Mehmet Remzi Dokmeci**[a,b,c], **Anthony Atala**[d], & **Ali Khademhosseini**[a,b,c,q,r,*]

[a]Biomaterials Innovation Research Center, Division of Engineering in Medicine, Department of Medicine, Brigham and Women's Hospital, Harvard Medical School, Boston, MA 02139, USA
[b]Harvard-MIT Division of Health Sciences and Technology, Cambridge, MA 02139, USA
[c]Wyss Institute for Biologically Inspired Engineering, Harvard University, Boston, MA 02115, USA
[d]Wake Forest Institute for Regenerative Medicine, Wake Forest School of Medicine, Medical Center Boulevard, Winston-Salem, NC, 27157, USA
[e]Department of Biomedical Engineering, Faculty of Engineering and Architecture, Izmir Katip Celebi University, Izmir 35620, Turkey
[f]Orthopaedic Research Center, Mashhad University of Medical Sciences, Mashhad 9176699199, Iran
[g]Graduate School Program in Biomedicine, Universidad de los Andes, Santiago 7620001, Chile
[h]Biosensor National Special Laboratory, Key Laboratory of Biomedical Engineering of Education Ministry, Department of Biomedical Engineering, Zhejiang University, Hangzhou 310027, P. R. China
[i]Metallurgical and Materials Engineering Department, Faculty of Engineering and Architecture, Eskisehir Osmangazi University, Eskisehir 26030, Turkey
[j]Institutes of Biomedical Sciences, Fudan University, Shanghai 200032, P. R. China
[k]Department of Electronics and Telecommunications, Polytechnic University of Turin, Turin, 10129, Italy
[l]BioMEMS and Bioinspired Microfluidics Laboratory, Center for Bioengineering Research and Education, Department of Mechanical and Manufacturing Engineering, University of Calgary, Calgary, Alberta T2N 1N4, Canada
[m]Department of Marine Science, Iranian National Institute for Oceanography and Atmospheric Science, Tehran 1411813389, Iran

[n]Division of Engineering Science, Faculty of Applied Science and Engineering, University of Toronto, Toronto, ON M5S 1A4, Canada
[o]Doctoral Program in Experimental Biology and Biomedicine, Center for Neuroscience and Cell Biology, Institute for Interdisciplinary Research, University of Coimbra, Coimbra 3030-789, Portugal
[p]Department of Electrical Engineering, Sahand University of Technology, Tabriz 5331711111, Iran
[q]Department of Bioindustrial Technologies, College of Animal Bioscience and Technology, Konkuk University, Seoul 143-701, Republic of Korea
[r]Department of Physics, King Abdulaziz University, Jeddah 21569, Saudi Arabia

*Corresponding authors.
Yu Shrike Zhang, Division of Engineering in Medicine, Department of Medicine, Brigham and Women's Hospital, Harvard Medical School, 65 Landsdowne Street, PRB 252, Cambridge, MA 02139, USA. Email: yszhang@research.bwh.harvard.edu
Ali Khademhosseini, Division of Engineering in Medicine, Department of Medicine, Brigham and Women's Hospital, Harvard Medical School, 65 Landsdowne Street, PRB 252, Cambridge, MA 02139, USA. E-mail: alik@bwh.harvard.edu

[†]Y.S.Z., J.A., and S.R.S. contributed equally to this work as primary author.

METHODS

Fabrication of breadboard

The breadboard was built using PDMS (Sylgard 184 silicone elastomer and curing agent, Dow Corning) and had a three-layer configuration including a pneumatic layer, a thin membrane, and a microfluidic layer, all bonded together irreversibly with air plasma treatment. Fabrication of the 20-μm thick PDMS membrane layer was achieved by spin coating and served as the pneumatic microfluidic valve (1). Both microfluidic channel (300 μm in height and width) and pneumatic channel (100 μm in height and 300 μm in width) were fabricated using a standard photolithography technique based on SU-8 50 (MicroChem). Subsequently the microfluidic layer master mold was converted to a convex hemicylindrical secondary mold (**Fig. S3**) (2). Briefly, a primary PDMS device was generated by molding, and then bonded to a 20-μm PDMS membrane in contact with the side of the channels. A SU-8 precursor was smeared evenly on a glass slide and covered by the membrane side of the primary PDMS mold from the top. A vacuum system was connected to the PDMS primary mold, generating a negative pressure to deform the membrane into the convex hemicylindrical shape inside the microchannels, incurving the SU-8 into the membrane. The SU-8 was then UV-cured from the top and subsequently used to fabricate the final hemicylindrical microfluidic layer.

Fabrication of microbioreactor

The microbioreactor was fabricated with PDMS (**Fig. S21**), consisting of a microfluidic perfusion layer at the top, and a chamber layer at the bottom bonded to a piece of glass treated with 3-(trimethoxysilyl)propyl methacrylate (TMSPMA) (Sigma-Aldrich). This microbioreactor was then cushioned with a 1-mm thick PDMS layer at the bottom and sandwiched between a pair of transparent PMMA (McMaster Carr) clamps to ensure hydraulic tightness. The microfluidic perfusion layer was fabricated by soft lithography using a positive 1.5 mm-thick mold of PMMA attached to a Petri dish. Once cured the PDMS device was punched with inlet and outlet to connect with Tygon microbore tubing and secured utilizing epoxy (Devcon). The chamber layer was fabricated by spin coating a 100-μm PDMS layer on TMSPMA treated glass. The 7 mm × 7 mm organoid chamber was cut out with a blade, exposing the glass surface. The microbioreactor was designed in a resealable manner to allow for opening and closing of the system for organoid patterning and sampling when necessary.

Fabrication of bubble trap

The bubble trap featured a 10-mm single-chamber containing microposts with a series of uniform diameters of 1000, 500, and 250 μm (with spacing identical to post diameter), and a height of 200 μm, leading to a total chamber volume of approximately 20 μL (**Fig. S5A**). The aligned posts in the fluidic layer are expected to prevent the bubbles from passing by to downstream both as physical barriers and through hydrophobic interactions. A vacuum chamber was further added on top of the fluidic chamber featuring the same array of microposts but a height of 100 μm and reduced length of side channels (**Fig. S5B**). Initially the gas bubbles can be captured by the microposts as soon as they enter the device with the fluid stream, due to both the physical confinement and the hydrophobic interactions between the bubbles and the PDMS surfaces. Under the negative pressure from the vacuum chamber the bubble elimination process immediately begins due to the gas permeability of the thin PDMS membrane (3, 4). The gas continuously passes through the PDMS membrane to reach the vacuum chamber and is eliminated until the entire volume of the bubbles is removed. Only the entrapped gas bubbles within the fluid chamber can be eliminated but not the atmospheric air from the other side of the device due to the sealing of the external surface by the PMMA clamps (**Fig. 2D, E**).

Fabrication of reservoir

The reservoirs for media and chemicals were fabricated using cryovials or centrifuge tubes (2, 5, 15, and 50 mL; Thermo Scientific) that were punched in the cap. The outlet consisted of Teflon tubing (0.020" × 0.060" OD; Cole-Parmer) inserted all the way to the bottom of the tube. The inlet had a stainless steel catheter coupler (Instech) inserted on the cap linked to the same Teflon tubing or a Tygon microbore tubing (0.012" ID × 0.030" OD; Cole-Parmer). Each connection was sealed by epoxy.

Fabrication of microelectrode set

The microelectrode set was composed of three electrodes: Au WE, Au CE, and Ag RE. The diameter of the WE was 800 μm, the width of CE and RE were both 150 μm, the gap between WE and other two electrodes was 200 μm, and the diameter of detection area was about 1500 μm (**Fig. S12**). The glass substrate was diced to specific dimensions using a dicing saw machine. The

diced glass chips were cleaned by acetone, isopropyl alcohol, and DI water and dried at 120 °C in an oven. The shadow mask of 0.25 mm in thickness was attached to the glass substrate. Subsequently, 20 nm-thick Ti, 20 nm-thick Pd, and 500 nm-thick Au were selectively deposited on the glass using the shadow mask using an electron beam evaporator to create the WE and CE. Then, the second shadow mask for RE patterning was attached to the Au-deposited glass substrate. In the same manner, 20 nm-thick Ti, 20 nm-thick Pd, and 500 nm-thick Ag were deposited on the glass substrate. Finally, the electrodes were annealed at 300 °C for 6 h in a furnace. Scanning electron microscopy (SEM, Zeiss) and atomic force microscopy (AFM, Bruker Corporation) were used to characterize the surface of Au electrode.

Integration of the microelectrode set with microfluidic electrochemical sensing chip

The microfluidic electrochemical sensing chip was fabricated using the same procedure with that for the breadboard. Three different types of chips were designed for desired uses (see main text; **Fig. 3C and D, and Fig. S15**). The microelectrode set was bonded to the chip using air plasma with the detection area aligning with the chamber. The three leads of the microelectrode set were coated with silver epoxy (MG Chemicals) to make electrical contact with copper wires for measurement.

To functionalize the microelectrode, the surface was first cleaned *via* a two-step electrochemical process that is detailed in the electrode regeneration section below. After the electrode cleaning, SAM formation, SPV immobilization, biotinylated antibody immobilization, and medium blocking were performed sequentially to complete functionalization (**Fig. 3A**). SAM formation was achieved by incubating 10 mM 11-MUA in ethanol (Sigma-Aldrich) to introduce carboxyl groups onto the surface. SPV was then immobilized to 11-MUA through carbodiimide reaction in the presence of NHS/EDC (50 mM each dissolved in 50 mM citric acid buffer at pH 4.5). Afterwards biotinylated antibodies of interest were conjugated onto the SPV layer through the biotin-SPV bonding by incubation. As a last step of functionalization process, the surface was blocked by incubating with the medium to prevent non-specific binding of other proteins. The duration of flow for each solution except 11-MUA and ethanol (10 min each) was 7 min and the duration of each incubation was 1 h except NHS/EDC and the medium (30 min each). After each incubation step, a washing step was performed. Before SPV incubation, the microelectrode was washed using PBS; after 11-MUA incubation, ethanol washing was followed

by PBS washing, while no washing was done after NHS/EDC incubation; and after SPV incubation, a 1X washing buffer of standard ELISA kits was utilized for washing.

Electrochemical detection of biomarkers

EIS measurements were conducted using the CHI660e electrochemical workstation (CHI Instruments) in a 50 mM $K_3Fe(CN)_6$ solution. The EIS signals were recorded in the frequency range of 0.1–10^5 Hz. The amplitude of the applied sine wave potential was 5 mV with the direct current potential set at 0.1 V. The EIS results were plotted as complex plane diagrams (*i.e.*, Nyquist plots). The evaluation of charge transfer resistance R_{ct} value was determined by simulating the data according to Randles circuit consisting of charge transfer resistance R_{ct}, solution resistance R_s, double-layer capacitance, C_{dl}, and Warburg impedance, W (5).

Regeneration of microelectrode set-integrated PDMS microfluidic chip

To achieve long-term monitoring, the saturated microelectrode surface was regenerated *via* a two-step electrochemical cleaning process: 10 mM H_2SO_4 followed by 50 mM $K_3Fe(CN)_6$. The H_2SO_4 cleaning was performed between the electrical sweep potentials of 0.0 V and 1.8 V, where the scan rate, sensitivity, and sample interval were set to 100 mV s^{-1}, 10^{-2} A/V, and 0.001 V, respectively. The $K_3Fe(CN)_6$ cleaning was carried out between potentials of 1.0 V and 0.0 V at scan rate of 200 mV s^{-1}, sensitivity of 10^{-4} A/V, and sample interval of 0.001 V. During the cleaning procedure the solutions were kept flowing at a rate of 1000 μL h^{-1}. The oxidation peak current of $K_3Fe(CN)_6$ as well as R_{ct} of the bare microelectrode were compared before and after regeneration to assess the stability and sensitivity of the regenerated microelectrode.

Physical sensors

The physical module housed the integrated pH and oxygen sensors (**Fig. S20A**). The pH sensor detected changes in the light absorption of phenol red (Sigma-Aldrich) in the medium (**Fig. S20B**) to translate into a voltage change (**Fig. S20C**). The light source consisted of a broadband light emitting diode (LED) (LEDWE-15, Thorlabs) fixed above the detection channel. Optical signal detection was achieved through a Si photodiode (FDS100, Thorlabs) fixed below the fluidic channel with a long-pass optical filter (FGL515, >515 nm, Thorlabs).

Oxygen-quenchable luminescent dye, $[Ru(dpp)_3]^{2+}Cl_2$–tris(4,7-diphenyl-1,10-phenanthroline)ruthenium(II) chloride (Sigma-Aldrich) with an excitation wavelength at 463 nm and a maximum emission at 618 nm, was deposited at the bottom of the chamber. The ruthenium powder was dissolved in ethanol (1 mg mL^{-1}). The dye was covered with a thin PDMS membrane obtained *via* spin coating at 6000 rpm for 1 min, allowing a physical barrier between the medium and the dye with oxygen diffusion. The dye was excited with a high-power blue LED (M470L3, 470 nm, 650 mW, Thorlabs) on top of the microfluidic channel with a band pass excitation filter (FGB7, 435–500 nm, Thorlabs) in between. Two Si photodiodes (FDS100) were fixed below the detection channel and filtered by a long pass filter (FGL610, 610 nm, Thorlabs) mounted above the photodiode. The oxygen signal was differentially recorded between the luminescent intensity from the dye and the background (**Fig. S20E**).

The detection channel was manufactured with PDMS (30 mm × 2 mm × 1 mm). The whole detection channel was sandwiched between two black PMMA with inlet, outlet, and light source holes to reduce interference from ambient light (**Fig. S20A**).

The temperature sensor used a Physitemp IT-18 Type T Thermocouple Probe (diameter: 0.025"; range: 0-150 °C; response time: 0.1 s) connected with a USB-TC01 Thermocouple Measurement Device (National Instruments). A flow rate sensor (Dolomite Mitos 3200098; range: 60–3000 μL h^{-1}; accuracy: 5%; response time: 30 ms) was also incorporated into the integrated system to monitor the flow rate and potential channel blockage and leakage.

Construction of the automation controller

The automation controller was constructed using a set of WAGO controllers and FESTO solenoid valves connected to a nitrogen gas source, where each of the valves could be individually actuated using custom-coded MATLAB (Mathworks) programs to control injection or microvalve function on the microfluidic chips (**Fig. S1**) (6). Injection valves were connected to the inlet of the chemical reservoirs. Microvalves were closed by purging N_2 through the solenoid resulting in bending of the thin PDMS membrane and closure of the corresponding microfluidic channel. The injection solenoid purged N_2 into the reservoir and the increased pressure would push the solution through the outlet of the reservoir. Synchronized operations of the microvalves and reservoirs led to injection of fluid into the desired channel of the chip.

Cell culture and patterning

Human primary hepatocytes were maintained in the Hepatocyte Maintenance Medium (both from Triangle Research Labs). HepG2 cells (ATCC) were maintained in Dulbecco's modified Eagle medium (DMEM, ThermoFisher) supplemented with 10 vol.% fetal bovine serum (FBS, ThermoFisher) and 1 vol.% penicillin-streptomycin (ThermoFisher). Patterning was achieved by adding 50 µL cell suspension containing 9×10^5 cells in 10 wt.% GelMA in PBS into the chamber layer of the microbioreactor. A photomask with a hepatic lobule-like arrangement (**Fig. S22A**) was placed on top of the GelMA and crosslinked by UV light (850 mW for 35 s, OmniCure S2000, Excelitas Technologies). The microbioreactor was immediately closed, placed in an incubator at 37 °C and perfused with medium.

Human iPSC-CMs (Stem Cell Theranostics) were thawed and directly seeded onto the GelMA pattern. The pattern was created by placing a photomask containing an aligned pattern of 75 µm in width and 75 µm spaced (**Fig. S22B**) (7) on top of 50 µL of 5 wt.% GelMA in PBS. UV light was used to crosslink the GelMA at 850 mW for 40 s. The iPSC-CMs were directly seeded onto the GelMA pattern at a density of 3×10^5 cells per chamber in 20–30 µL to allow for their sedimentation and attachment for at least 2 h. Afterwards, a PBS solution containing freshly mixed 30 mg mL^{-1} fibronogen and 10 U mL^{-1} thrombin (Sigma-Aldrich) was then gently added onto each pattern seeded with iPSC-CMs and incubated for an additional 30 min at 37 °C to allow the formation of a fibrin gel to protect the iPSC-CMs from direct exposure to the fluid flow. The cardiac organoids were cultured with RPMI 1640 (ThermoFisher) supplemented with 1X B27 (ThermoFisher) at 37 °C with 5% CO_2 for 2–4 days until beating of the cells was detected. The chamber layer was then sealed with the microfluidic layer to complete the cardiac microbioreactor.

Common media were prepared to meet the needs of co-cultures in the integrated system when necessary. For the heart-and-liver system, a cardiac basal medium composed of RPMI 1640 and Hepatocyte Maintenance Medium mixed in a 1:1 proportion was reconstituted; after this common basal medium was created, 1X B27 supplement and the supplements provided by Triangle Research Labs were added. For the heart-and-liver-cancer system, RPMI 1640 and DMEM were reconstituted at 1:1 ratio and supplemented with 10 vol.% FBS. Both common media were found to sustain sufficient viability and functionality of the cells types required to perform further experiments.

Cell viability was assessed with a LIVE/DEAD® viability/cytotoxicity kit (ThermoFisher). Sarcomeric α-actinin and connexin-43 were stained using a standard immunofluorescence protocol (primary antibodies: ab9465 and ab11370, respectively, Abcam; secondary antibodies: Alexa 568 anti-mouse and Alexa 488 anti-rabbit, respectively, ThermoFisher). The Zeiss Axio Observer D1 Fluorescence Microscope (Carl Zeiss) was used to capture all images and ImageJ was used for image analysis.

Organoid scaling and fluidics

Scaling of the organoids was calculated according to cell density per organ (8). Given that for the human heart contains approximately 20×10^6 cells and hepatocyte number in the liver varies at $25–139\times10^6$ (averaging 77×10^6 cells), the organoids were constructed roughly under the same proportion, *i.e.*, 3×10^5 cells for the cardiac organoid and 9×10^5 cells for the primary liver organoid.

The overall volume of a typical integrated system, including two bioreactors, a bubble trap, an electrochemical sensing module, a physical sensing module, a medium reservoir, connecting tubing, and microchannels of the breadboard, was 5 mL. This volume was scaled according to a millihuman system considering a total blood volume of roughly 4.85×10^3 mL in human (8), and approximated to 5 mL. This volume was also experimentally validated to sustain a 5-day culture of the dual-organoid platform without the need for changing the medium. The tubing had a total length of approximately 600 mm (circular with an inner diameter of 0.508 mm) for connecting fluidic components together; the length of tubing used for connecting the peristaltic pump to the fluidic circuitry was approximately 290 mm (circular with an inner diameter of 0.76 mm); and the length of microchannels in the breadboard was approximately 124 mm (hemicylindrical with a diameter of 0.3 mm).

The flow rate of the medium was set at 200 μL h^{-1}. This rate was chosen according to our previously established protocol for a liver bioreactor (9), showing that a flow rate of higher than 200 μL h^{-1} allowed for sufficient oxygen consumption by the hepatocytes. In addition, this flow rate is low enough to avoid untypical high shear stress in the bioreactors experienced directly by both the liver and cardiac organoids (10). The maximum Reynolds number of the system was calculated to be 0.13, which belonged to the tubing with the inner diameter of 0.508 mm. Thus, the flow regime was considered laminar through the whole fluidic circuit.

Mini-microscope

To monitor the behaviors of the organoids inside the microbioreactors *in situ*, a webcam (Logitech C160)-based mini-microscope was fabricated and fixed at the bottom of the microbioreactors (**Fig. S20I**). To analyze the beating of cardiac organoids, a set of custom-written MATLAB code was used to extract the intensity change or pixel shift of the captured video to achieve real-time contraction assessment (11).

Integration of dual-organ-on-chip system

A PMMA base was designed to modularly host the major components including the breadboard, microbioreactors, physical sensors, electrochemical immunobiosensors, bubble traps, and the reservoir. The pneumatic layers of all the microfluidic chips were connected using Teflon tubing (0.020" ID × 0.060" OD) by 215 G × 8 mm stainless steel catheter couplers (Instech) and secured with epoxy. Subsequently they were filled with food dyes and connected to the pneumatic system actuated by nitrogen gas. Food dyes were used to pre-fill the valve channels and eliminate possible entrance of gas into the microfluidic layer during the actuation of the valves. The microfluidic layers of all chips were channeled using Tygon microbore tubing (0.012" ID × 0.030" OD) and 27 G × 8 mm stainless steel catheter couplers (Instec) and secured with epoxy when necessary. The loop was closed by insertion of the outlet Tygon microbore tubing of the breadboard into the inlet of standard two-stop peristaltic tubing (Analytical West), and the outlet into the inlet of the medium reservoir (**Fig. 1B and Fig. S2**). The system was perfused using a peristaltic pump (MP^2, Cole-Parmer) at a flow rate of 200 μL h^{-1}.

Drug Treatment

Two drugs were selected to test the biomimetic human dual-organ-on-chip systems according to their target toxicity and differences amongst their adverse effects in the human body, which are detailed in the main text (**Figs. 5 and 6**). APAP (Sigma-Aldrich), a liver toxic drug, was administrated to the heart-and-liver-on-chip system at dosages of 0, 5, and 10 mM based on results obtained from our previous work (9). Literature has also suggested that safe doses of APAP in humans are approximately 2–5 mM (12), which fall in the range of the doses that we chose for testing hepatotoxicity. The drug was infused into the system at 72 h and the screening

was maintained for up to 120 h to probe its chronic toxicity towards the organoids. DOX (Sigma-Aldrich), a common chemotherapeutic drug, was used to evaluate toxicity in the heart-and-liver-cancer-on-chip system (13, 14). The doses of DOX for patients bearing cancer range from 20–75 mg m^{-2}; considering an adult having a surface area of approximately 1.6 m^2 the doses would then translate to roughly 12–36 μM (15). However, it has further been shown that the concentration of single-dose DOX administrated intravenously peaks at as low as approximately 0.9–3 mg mL^{-1}, or 1.7–5.5 μM. Therefore, doses of 0, 5, and 25 μM for DOX were chosen for studying its toxicity in our system. The drug was infused into the system at time 0 to probe its acute toxicity towards the organoids for up to 24 h. Physical sensors were kept running continuously and the medium was dynamically sampled at pre-defined time points for biomarker measurements using the electrochemical immunobiosensors. In addition, capecitabine (Sigma-Aldrich) at 80 μM was used to demonstrate the functionality of the human liver-and-heart-on-chips platform, while hyperthermia treatment *via* elevation of temperature of the incubation system to 41, 43, or 45 °C allowed for validation of the utility of the physical sensors to monitor environmental stimuli-induced changes in cell behaviors and consequent alteration in physical parameters.

Statistical analysis

Sigmaplot 12.0 and Graphpad 6.0 were used to perform statistical analysis of the experimental results. At least 3 samples were analyzed per group and a power analysis was used to determine the sample size prior to each experiment. For electrochemical measurements the samples were excluded from the analysis when leakages from the sensing chips were observed; otherwise all the data were included.

References

1. Kang E*, et al.* (2011) Digitally tunable physicochemical coding of material composition and topography in continuous microfibres. *Nat Mater* 10(11):877-883.
2. HoáLee K (2010) Novel PDMS cylindrical channels that generate coaxial flow, and application to fabrication of microfibers and particles. *Lab Chip* 10(14):1856-1861.
3. Singh A, Freeman BD, & Pinnau I (1998) Pure and mixed gas acetone/nitrogen permeation properties of polydimethylsiloxane [PDMS]. *J Polym Sci, Part B: Polym Phys* 36(2):289-301.
4. Merkel TC, Bondar VI, Nagai K, Freeman BD, & Pinnau I (2000) Gas sorption, diffusion, and permeation in poly(dimethylsiloxane). *J Polym Sci, Part B: Polym Phys* 38(3):415-434.

5. Randles JEB (1947) Kinetics of rapid electrode reactions. *Discuss Faraday Soc* 1:11-19.
6. Rafael's Microfluidics Site: https://sites.google.com/site/rafaelsmicrofluidicspage/.
7. Annabi N*, et al.* (2013) Highly elastic micropatterned hydrogel for engineering functional cardiac tissue. *Adv Funct Mater* 23(39):4950-4959.
8. Wikswo JP*, et al.* (2013) Scaling and systems biology for integrating multiple organs-on-a-chip. *Lab Chip* 13(18):3496-3511.
9. Bhise NS*, et al.* (2016) A Liver-on-a-Chip Platform with Bioprinted Hepatic Spheroids. *Biofabrication* 8(1):014101.
10. Maschmeyer I*, et al.* (2015) A four-organ-chip for interconnected long-term co-culture of human intestine, liver, skin and kidney equivalents. *Lab Chip* 15(12):2688-2699.
11. Zhang YS*, et al.* (2015) A cost-effective fluorescence mini-microscope for biomedical applications. *Lab Chip* 15(18):3661-3669.
12. Lee WM (2004) Acetaminophen and the US Acute Liver Failure Study Group: lowering the risks of hepatic failure. *Hepatology* 40(1):6-9.
13. Sadeghi-Aliabadi H, Minaiyan M, & Dabestan A (2010) Cytotoxic evaluation of doxorubicin in combination with simvastatin against human cancer cells. *Res Pharm Sci* 5(2):127-133.
14. Alami N*, et al.* (2007) Comparative analysis of xanafide cytotoxicity in breast cancer cell lines. *Br J Cancer* 97(1):58-64.
15. Creech RH, Catalano RB, & Shah MK (1980) An effective low‐dose adriamycin regimen as secondary chemotherapy for metastatic breast cancer patients. *Cancer* 46(3):433-437.

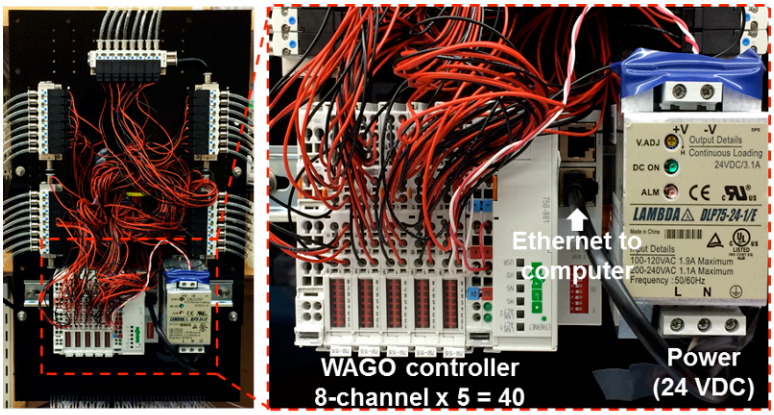

Fig. S1. Interior view of the Wago controller and Festo valve sets.

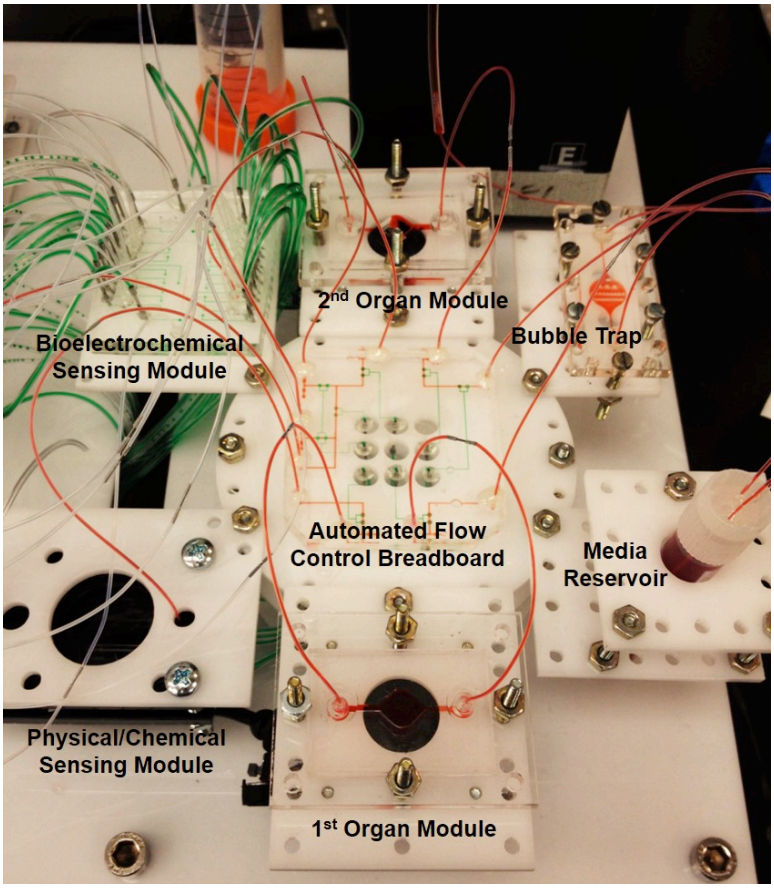

Fig. S2. Photograph of an integrated platform consisting of modular components including microbioreactors, breadboard, reservoir, bubble trap, physical sensors, and electrochemical biosensors.

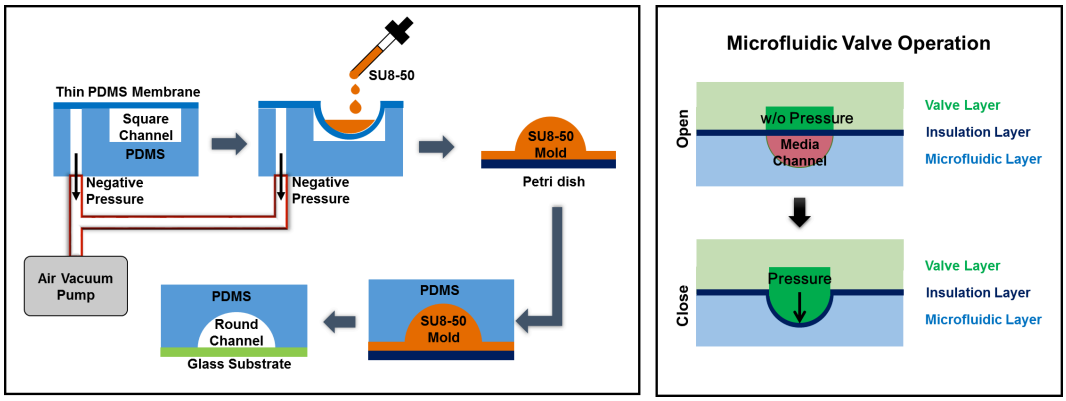

Fig. S3. Fabrication of round channel for microfluidic valve operation.

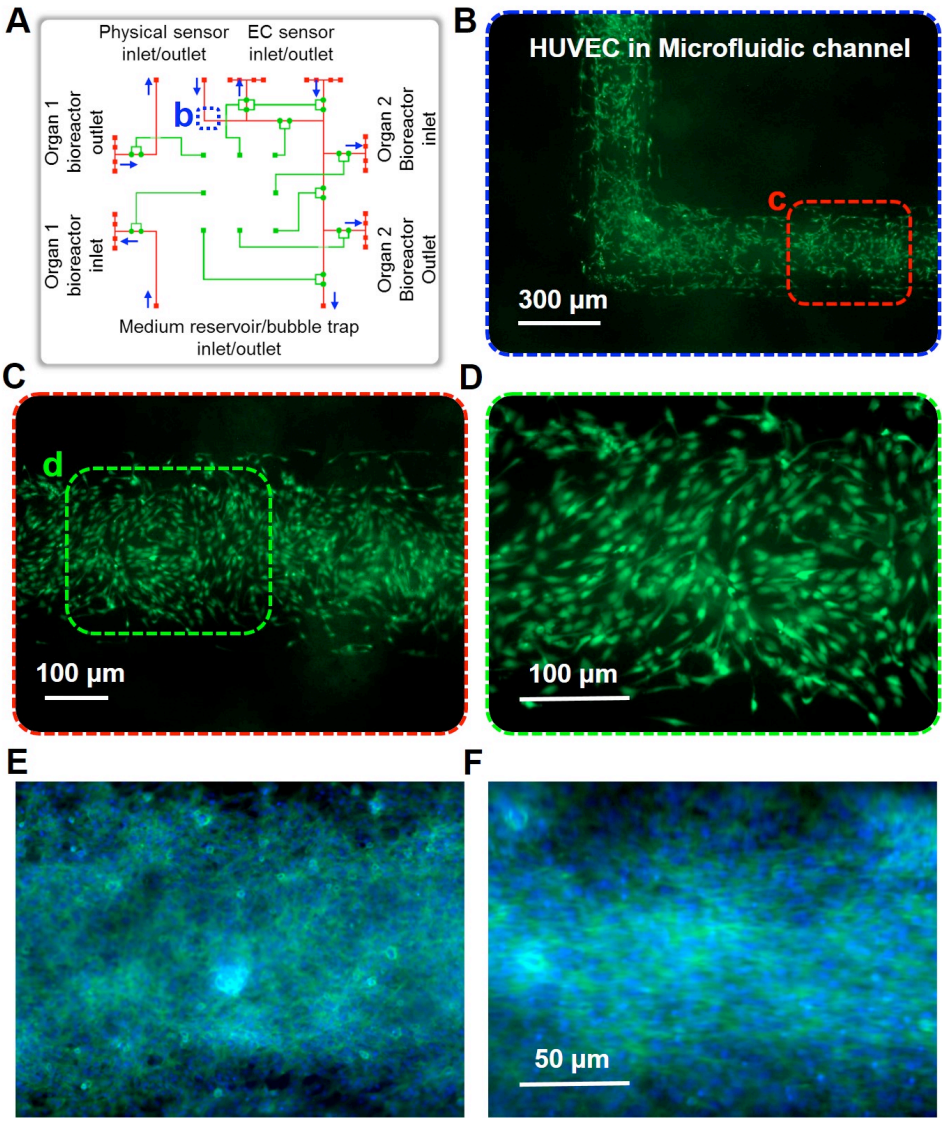

Fig. S4. HUVECs cultured in the microfluidic channels of breadboard. (**A**) Schematic of the breadboard. (**B–D**) HUVECs coated on the surface of the microfluidic channel of the breadboard at different magnifications after 7 days of culture, stained for cytoplasm with calcein. (**E, F**) HUVECs grown on the surface of the microfluidic channel of the breadboard after 14 days of culture (**E**) without and (**F**) under flow at a rate of 200 µL h^{-1}, stained for f-actin (green) and nuclei (blue).

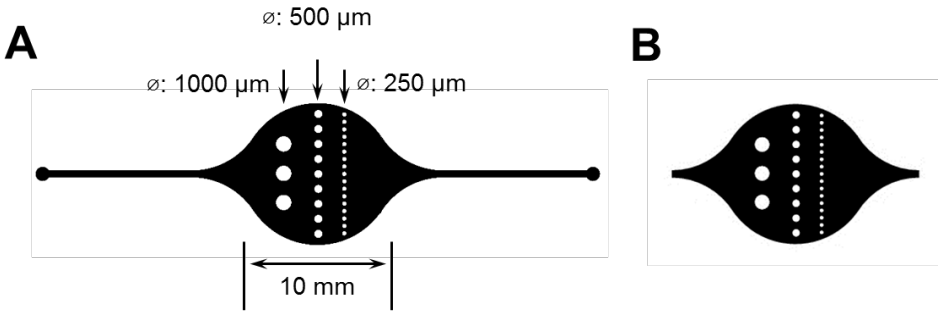

Fig. S5. Schematic diagrams showing design of the bubble trap, (**A**) fluidic layer at bottom with a thickness of 200 µm composed of arrays of microposts with different sizes (1000, 500, and 250 µm); (**B**) vacuum layer at the top with a thickness of 100 µm composed of the same arrangement of microposts.

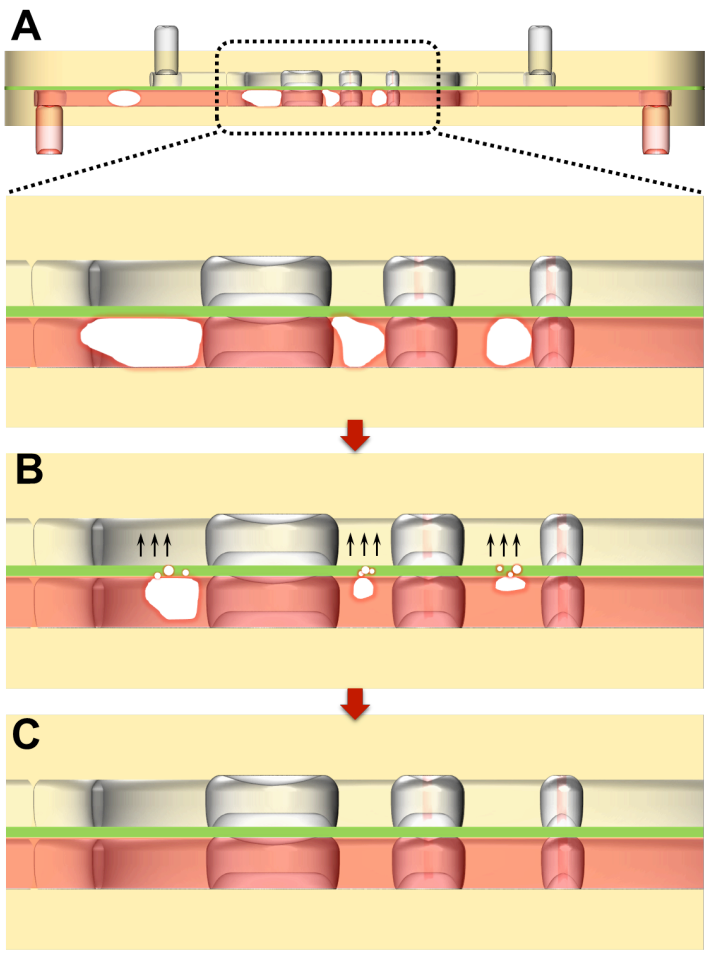

Fig. S6. Working principle of the bubble trap. (**A**) Schematics of gas bubbles captured by the microposts based on the physical confinement and the hydrophobic interactions between the bubbles and the PDMS surfaces. (**B, C**) The bubble elimination process under the negative pressure from the vacuum chamber based on the gas permeability of the thin PDMS membrane.

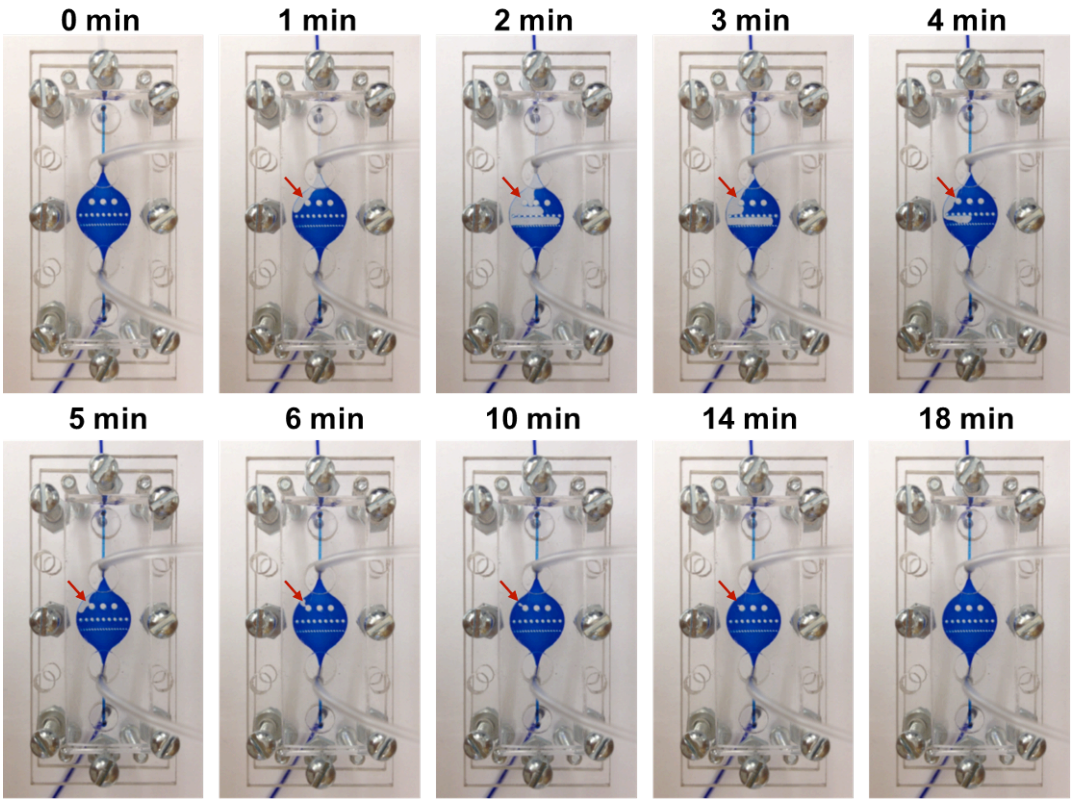

Fig. S7. Effective stop and elimination of bubbles by the bubble trap within 18 min.

Table S1. Quantification of bubbles in the microfluidic systems in the absence and presence of bubble traps. In this experiment, the bubble trap was integrated in a closed microfluidic circuit where flow was generated using a peristaltic pump set at a flow rate of 200 μL h^{-1}. The actual flow rate in this microfluidic circuit was subsequently measured using a flow sensor (which was placed downstream of the bubble trap in the case where there was a bubble trap). It was assumed that, the measured flow rates in the range of 100–300 μL h^{-1} were within the errors of the set flow rate (200 μL h^{-1}) due to the peristaltic movement of the pump, while those measured beyond 300 μL h^{-1} would be mainly caused by the presence of bubbles, with higher flow rates representing larger bubbles passing through the flow sensor. The data indicated successful elimination of gas bubbles in the microfluidic system when the bubble trap was used, at a set flow rate of 200 μL h^{-1} that has been used throughout all the experiments performed in the paper.

Conditions	**w/o Bubble Trap**		**w/ Bubble Trap**		**Reduction%**
Flow Rate (μL h^{-1})	**No. Spikes**	**Spikes%**	**No. Spikes**	**Spikes%**	
100-300	80406	85.70	93173	99.30	n/a
300-500	13701	13.93	636	0.68	95.13
500-800	260	0.28	19	0.02	92.69
800-1100	88	0.09	0	0.00	100
>1100	3	0.00	0	0.00	100

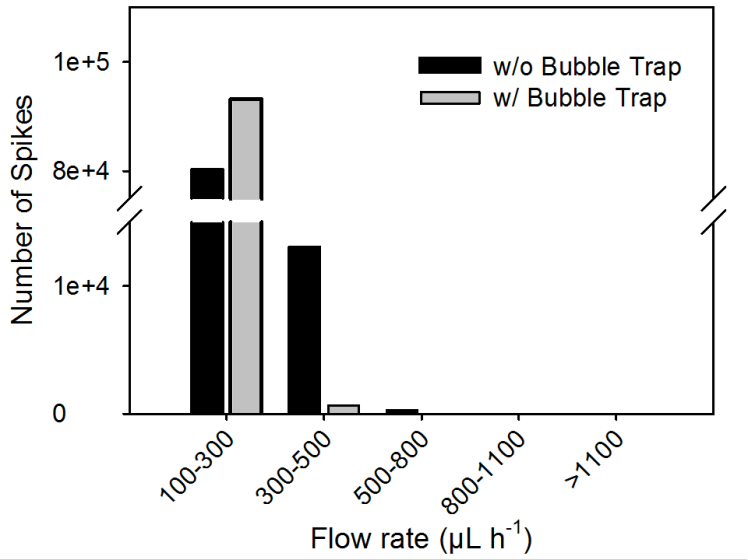

Fig. S8. Quantification of bubbles in the microfluidic systems in the absence and presence of bubble traps under different flow rates. The experiments were performed as described in **Table S1**.

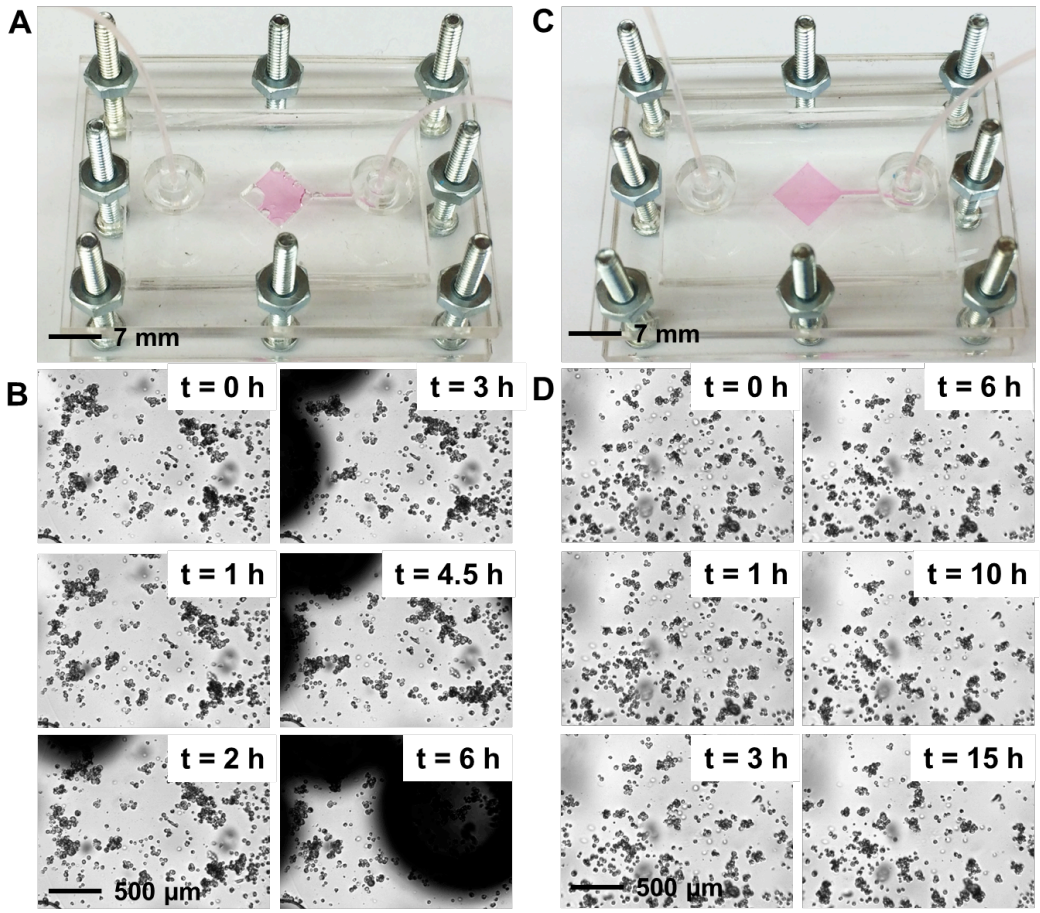

Fig. S9. Comparison of bubbles in the microbioreactors in the absence and presence of bubble trap. (**A, B**) The photographs of bubble accumulation in the microbioreactor without an upstream bubble trap. (**C, D**) The photographs of microbioreactor with an upstream bubble trap.

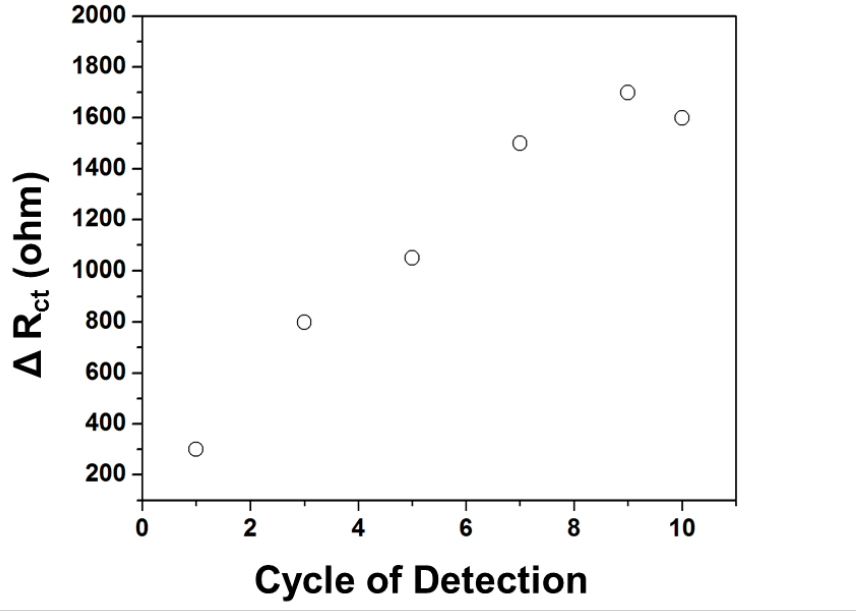

Fig. S10. Saturation of the electrode upon antigen (albumin) binding. The measurements were made on a single piece of electrode set, by incubating the same concentration (10 ng mL^{-1}) of albumin solution with the electrode surface in each detection cycle for up to 10 cycles, presented in the form of ΔR_{ct} value, which is the difference of the R_{ct} values obtained after each cycle and that obtained after medium blocking.

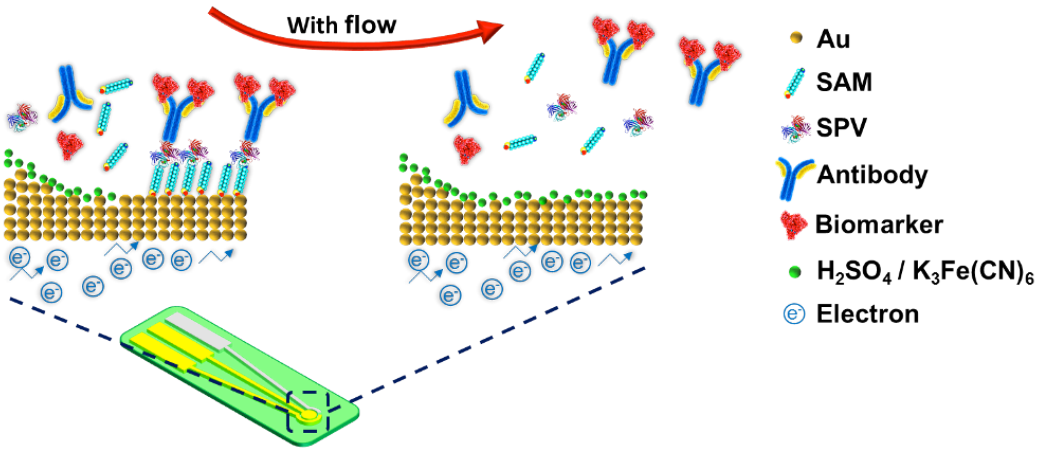

Fig. S11. Schematics showing the regeneration of the electrochemical immunobiosensor under fluidic flow.

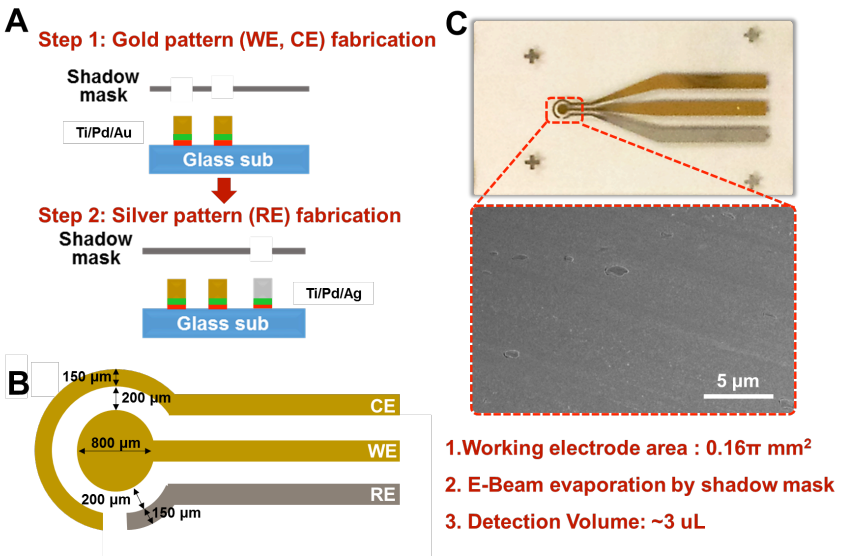

Fig. S12. Fabrication and characterization of the microelectrode set. (**A**) Two-step fabrication of Au (WE, CE) and Ag (RE) patterns on a glass substrate. The shadow mask of 0.25 mm in thickness was attached to a clean glass substrate; subsequently, 20 nm-thick Ti, 20 nm-thick Pd, and 500 nm-thick Au were selectively deposited onto the glass using the shadow mask by an electron beam evaporator to create the WE and CE; then, the second shadow mask for RE patterning was attached to the Au-deposited glass substrate to deposit 500 nm-thick Ag; finally, the electrodes were annealed at 300 °C for 6 h in a furnace. (B) Structural parameters of the microelectrode set: widths of all electrodes were 150 μm, diameter of the WE pad was 800 μm, and gaps between the WE and CE/RE were 200 μm. (C) Photograph of a fabricated microelectrode set and SEM image showing the surface of the WE.

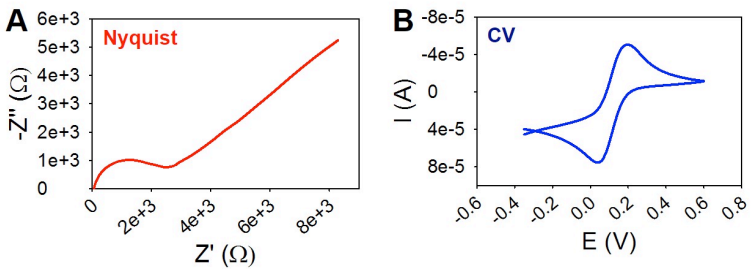

Fig. S13. Characteristic (**A**) EIS and (**B**) CV plots of a fresh microelectrode.

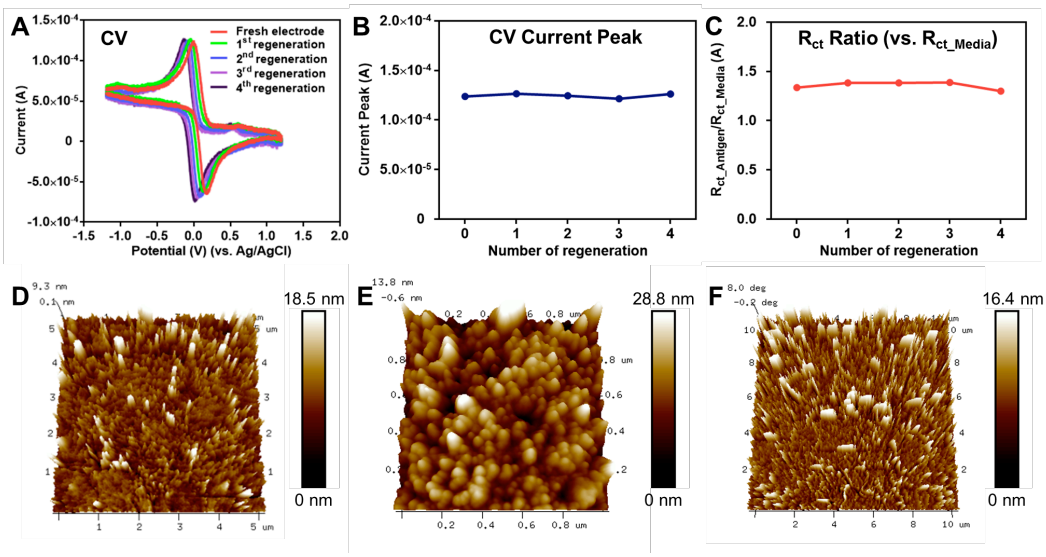

Fig. S14. Characterization of the electrochemical properties of the microelectrodes after regenerations. (**A, B**) Representative CV curves and current peaks of regenerated microelectrode in each cycle. (**C**) The R_{ct} Ratio of antigen detection (10 ng mL^{-1} albumin) after each regeneration cycles. (**D–F**) AFM images of the microelectrode surface after fabrication, functionalization, and regeneration.

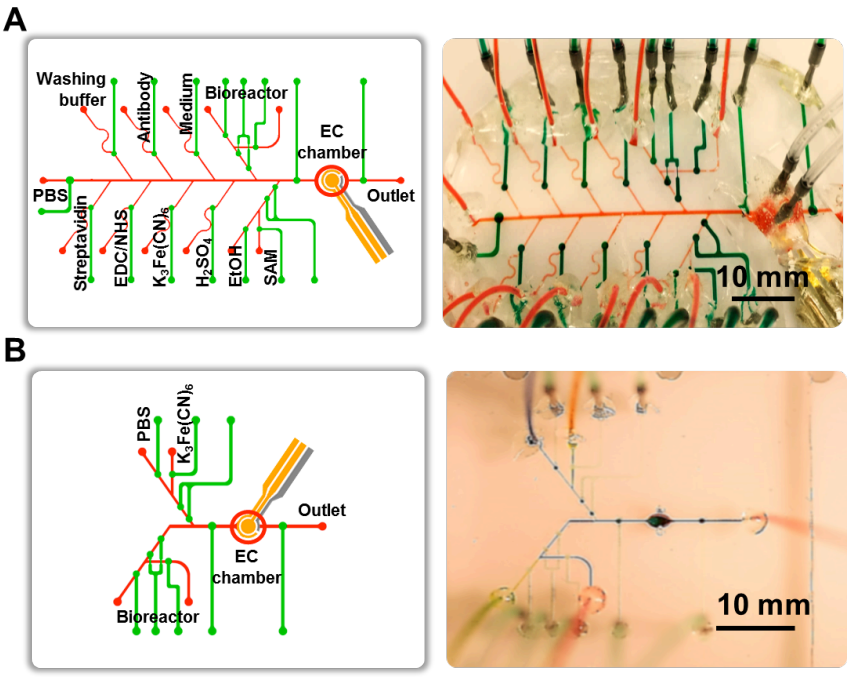

Fig. S15. Microfluidic chip-integrated electrochemical biosensors. (**A**) Automated regeneration microfluidic chip. (**B**) Single-use microfluidic chip.

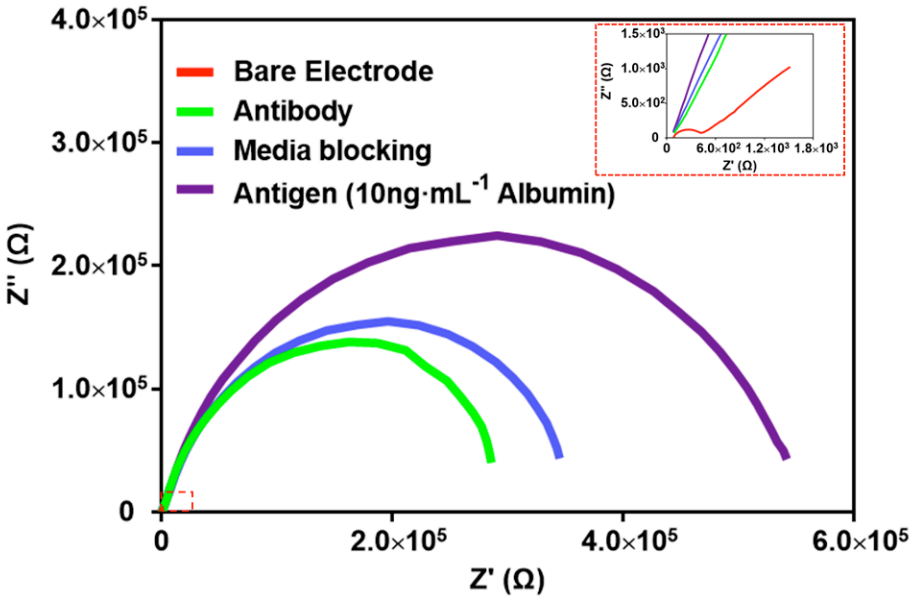

Fig. S16. Nyquist plots showing on-chip functionalization of the microfluidic electrochemical immunobiosensor. Inset with dash is the enlarged view from the dashed rectangle.

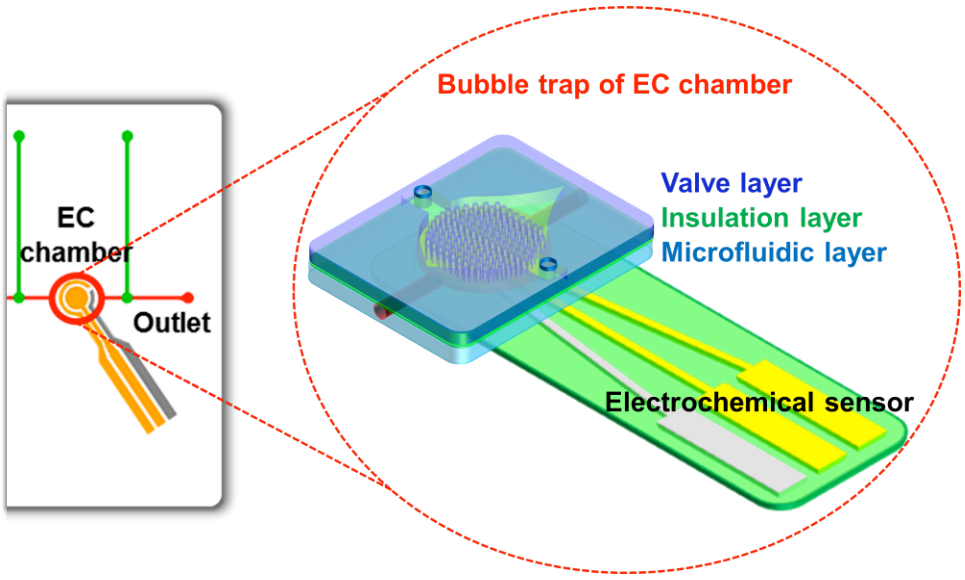

Fig. S17. Integration of a bubble trap directly on top of the electrochemical sensing chamber for efficient bubble removal.

Table S2: Comparison of detection ranges and LoDs of electrochemical sensors and ELISA assays for albumin, GST-α, and CK-MB.

Analyte	**Electrochemical sensor**		**ELISA**	
	Detection range (ng mL^{-1})	LOD (ng mL^{-1})	Detection range (ng mL^{-1})	LOD (ng mL^{-1})
Albumin	0.1–100	0.09	3.125–200	1.5
GST-α	0.1–100	0.01	0.313–20	0.188
CK-MB	0.01–10	0.0024	3.12–100	1.0

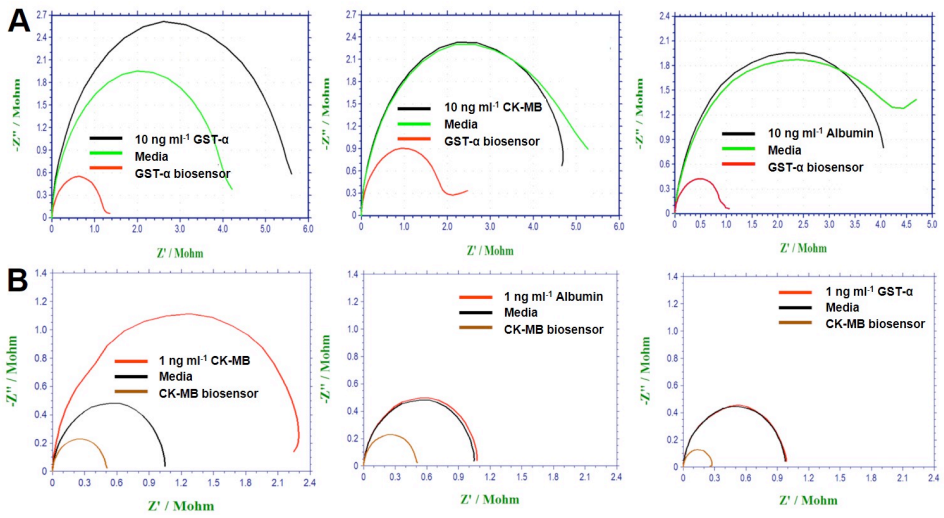

Fig. S18. Selectivity study of the GST-α and CK-MB biosensors. (A-C) Nyquist plots of impedance spectra obtained GST- α biosensor after the addition of (A) a specific antigen as GST-α (10 ng ml^{-1}) and two non-specific antigens as (B) CK-MB (10 ng ml^{-1}) and (C) Albumin (10 ng ml^{-1}). (D-F) Nyquist plots of impedance spectra obtained from electrodes functionalized for CK-MB aptamer after the addition of three different antigens such as (D) CK-MB (1 ng ml^{-1}), (E) Albumin (1 ng ml^{-1}) and (F) GST-α (1 ng ml^{-1}).

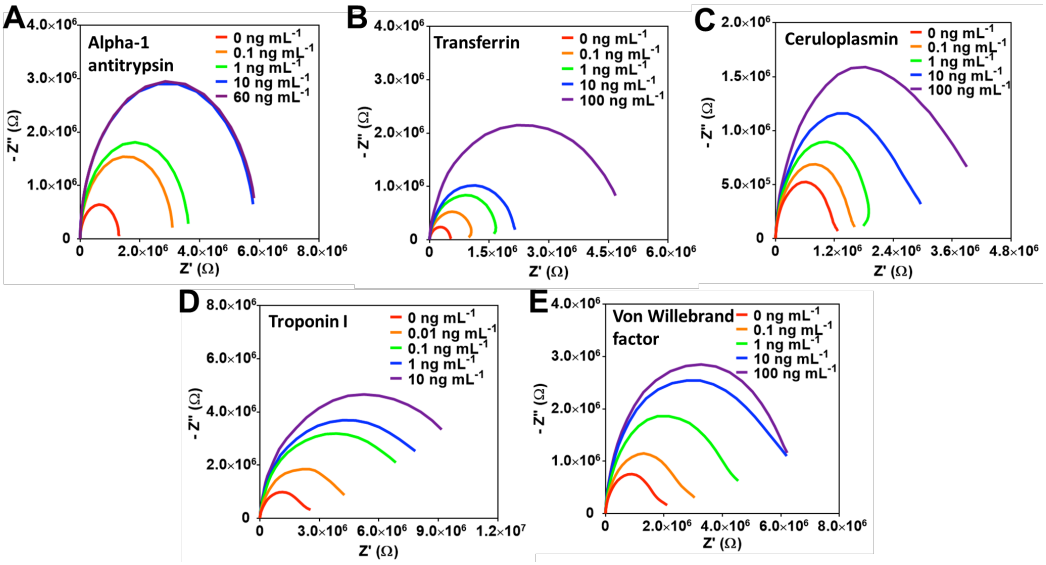

Fig. S19. Electrochemical detection of a panel of hepatic, cardiac, and vascular biomarkers. (**A**) Alpha-1 antitrypsin. (**B**) Transferrin. (**C**) Ceruloplasmin. (**D**) Troponin I. (**E**) von Willebrand factor.

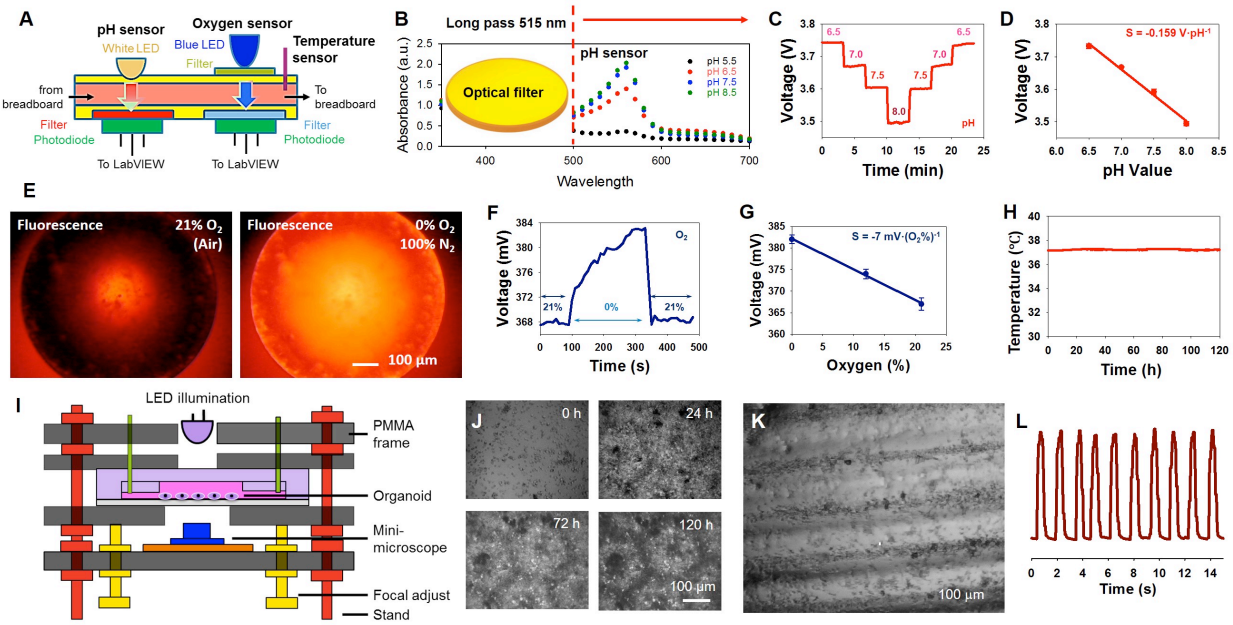

Fig. S20. (**A**) Schematic diagram showing the microfluidic pH, O_2, and temperature sensing unit. (**B**) Absorption spectra of phenol red under difference pH values at λ>515 nm. (**C, D**) Step plot and calibration curve for the optical pH sensor. (**E**) Fluorescence intensity of the ruthenium-embedded PDMS under different oxygen concentrations. (**F, G**) Step plot and calibration curve for the optical O_2 sensor. (**H**) Continuous temperature monitoring for 5 days. (**I**) Schematic diagram showing the mini-microscope that could be directly fitted at the bottom of a bioreactor. (**J**) Mini-microscopic images of the liver cancer organoid cultured inside the bioreactor for 120 h obtained from *in situ* observation. (**K**) Mini-microscopic image of the cardiac organoid cultured inside the bioreactor at 120 h obtained from *in situ* observation. (**L**) Real-time measurement of the beating of a human iPSC cardiac organoid with the mini-microscope. Detection principle of the physical optical sensors.

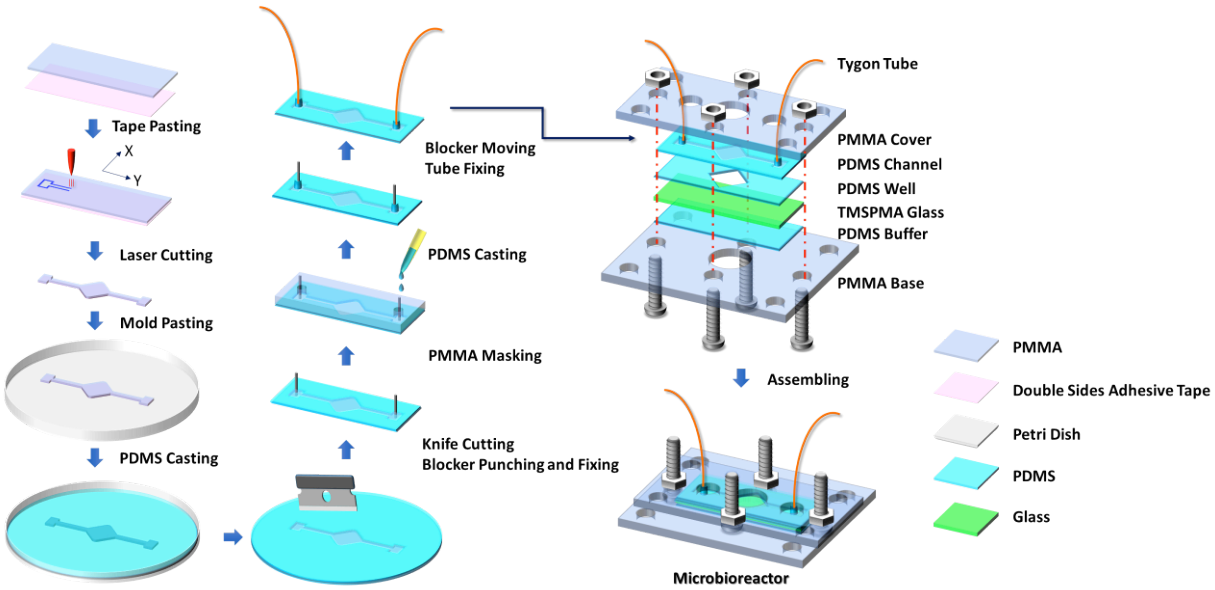

Fig. S21. Fabrication and assembly of the microbioreactor.

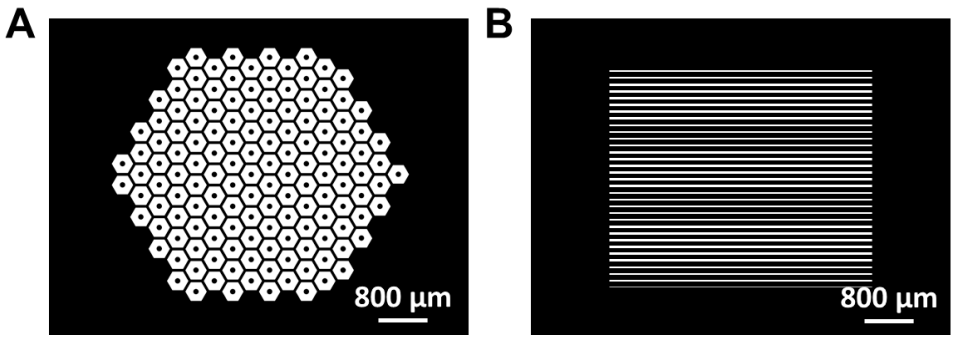

Fig. S22. Photomasks for GelMA patterning on the bottom of the microbioreactors. (**A**) Photomask of the hepatocyte pattern for hepatic lobule formation. (**B**) Photomask of line pattern for cardiomyocyte alignment.

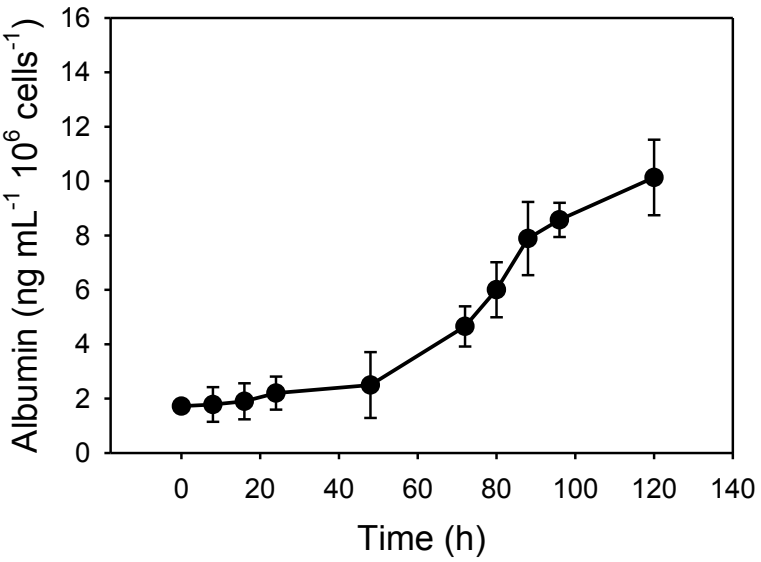

Fig. S23. Secretion of albumin from human primary liver organoids over a culture period of 5 days.

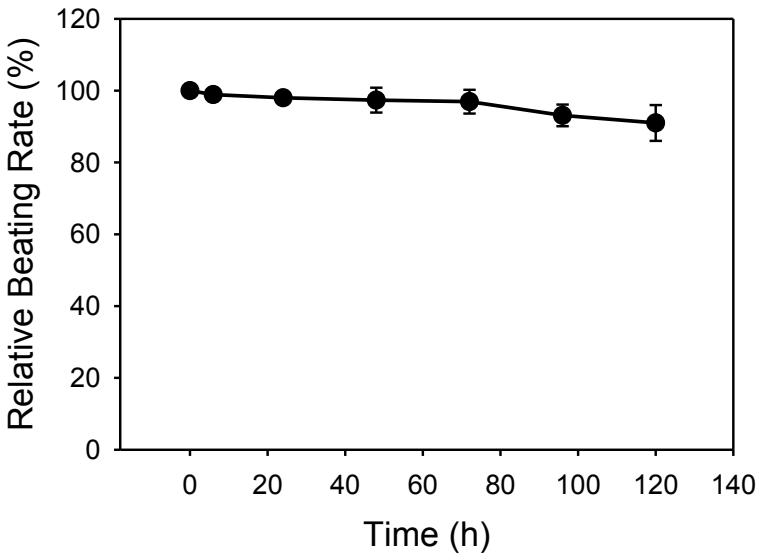

Fig. S24. Beating of human cardiac organoids over a culture period of 5 days.

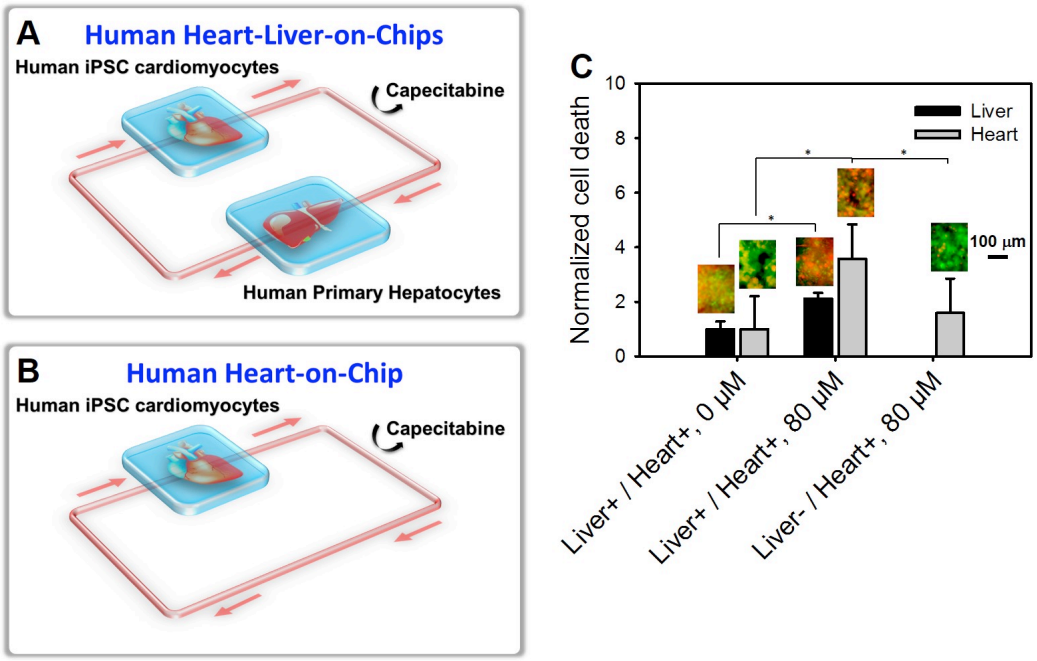

Fig. S25. Demonstration of dual-organ interactions in the integrated human liver-and-heart-on-chips platform. (**A, B**) Schematics showing a human liver-and-heart-on-chips platform and a human heart-on-chip platform challenged with 80 μM capecitabine, respectively. (**C**) Normalized cell death for hepatocytes and iPSC-CMs in the two platforms without and with capecitabine treatment. Enhanced cell death in the dual-organ system was likely attributed to the metabolism of capecitabine to 5-FU. *P<0.05.

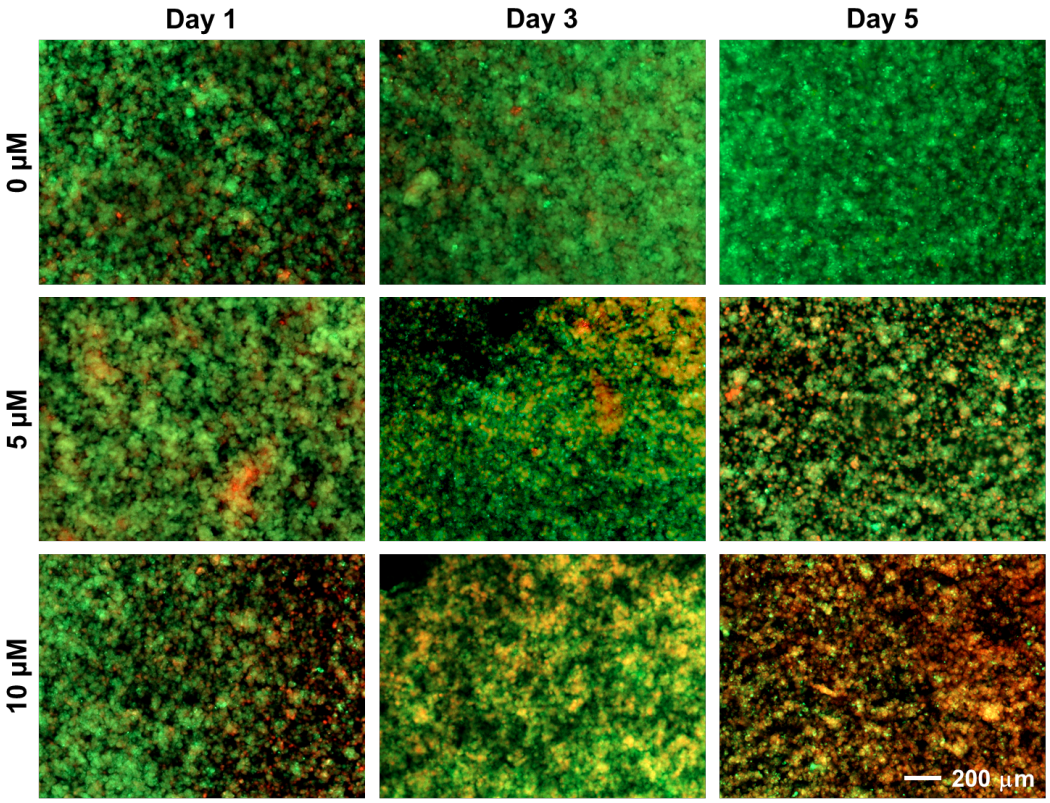

Fig. S26. Live/dead staining of the human primary hepatic organoids post treatment with 0, 5, and 10 mM APAP, at the end of 120 h. The APAP were introduced into the system at 72 h system integration.

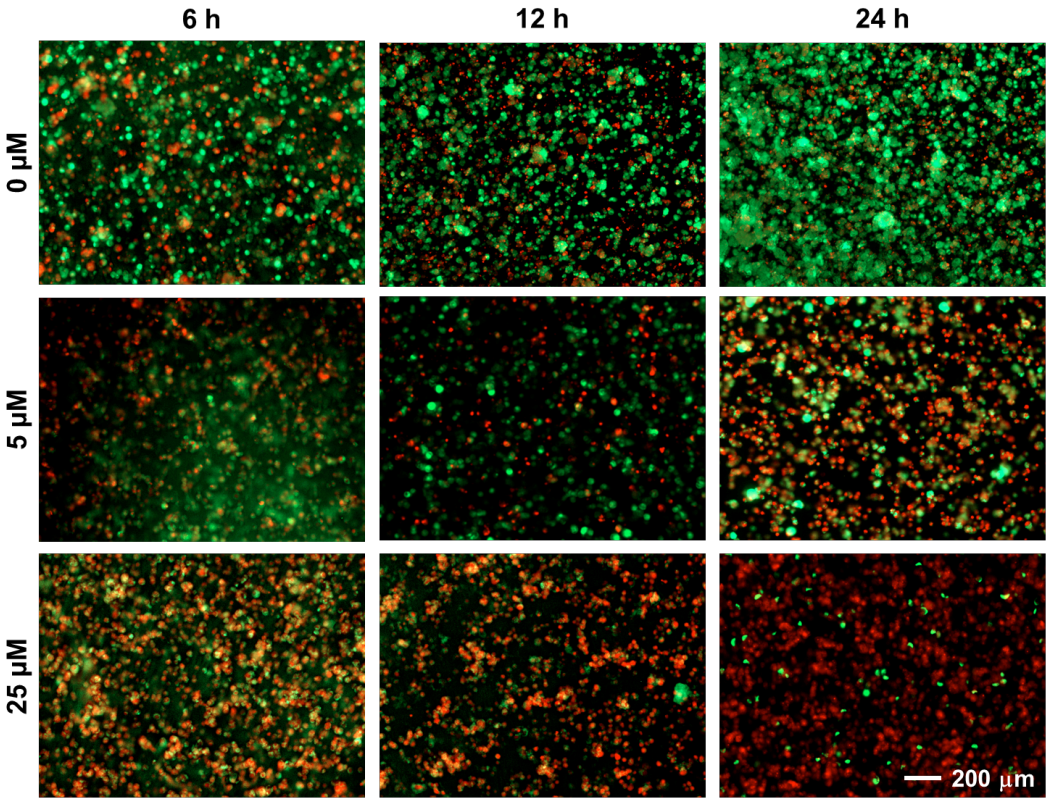

Fig. S27. Live/dead staining of the human liver cancer organoids post treatment with 0, 5, and 25 µM DOX, at the end of 24 h. The DOX were introduced into the system from time 0 post system integration.

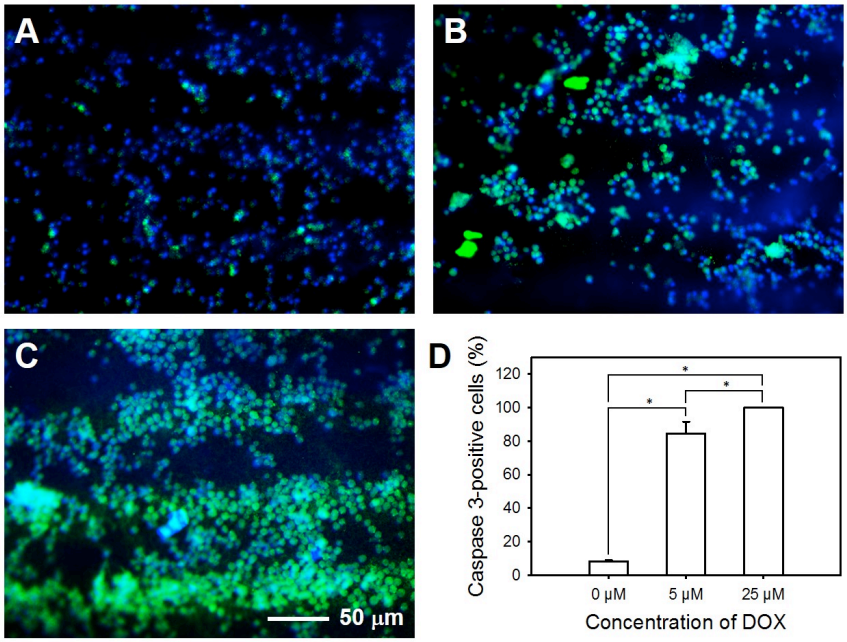

Fig. S28. Characterization of apoptosis of iPSC-CMs undergoing DOX treatment. (**A–C**) Fluorescence images showing caspase 3 (green) and nuclei staining (blue) of the cardiac organoids 24 h after treatment with DOX at 0, 5, and 25 μM, respectively. (**D**) Quantification of caspase 3-positive cells. N = 3, *$p<0.05$.

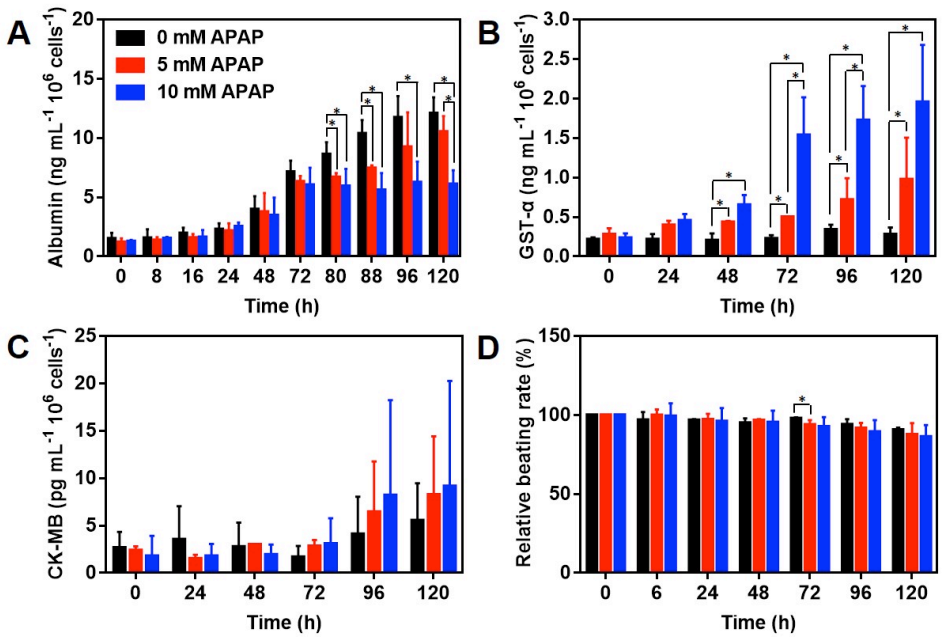

Fig. S29. Characterization of human heart-liver-on-chips post APAP treatment. (**A–C**) In-line automated electrochemical measurements of albumin and GST-α secreted from the hepatic organoids as well as CK-MB from the cardiac organoids. (**D**) Beating analysis of the cardiac organoids. Red arrows indicate the time when the drug was added (72 h). N = 3, *p<0.05.

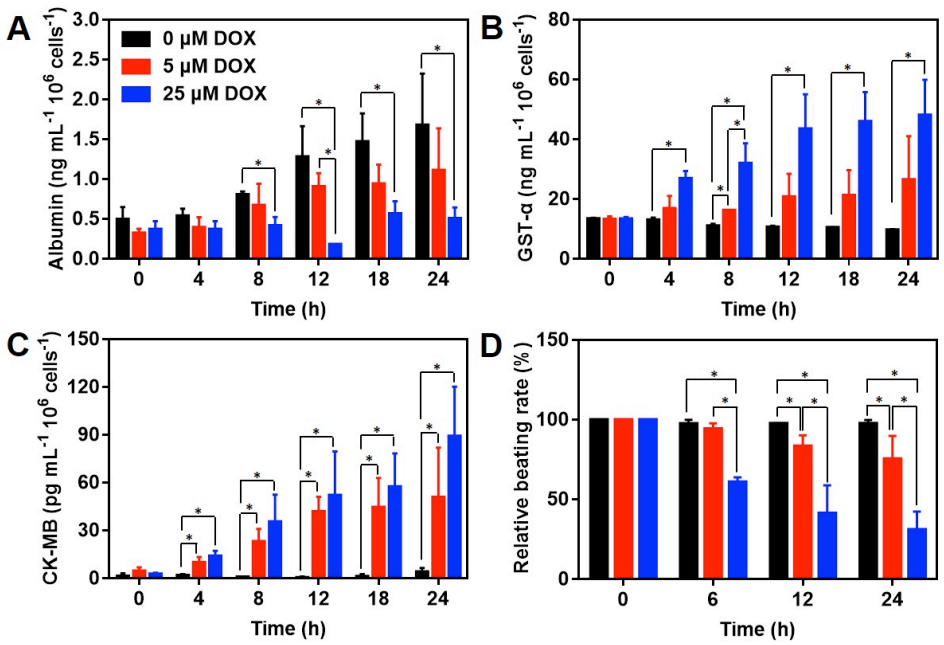

Fig. S30. Characterization of human heart-hepatoma-on-chips post DOX treatment. (**A–C**) In-line automated electrochemical measurements of albumin and GST-α secreted from the hepatic organoids and CK-MB from the cardiac organoids. (**D**) Beating analysis of the cardiac organoids. Red arrows indicate the time when the drug was added (72 h). N = 3, *p<0.05.

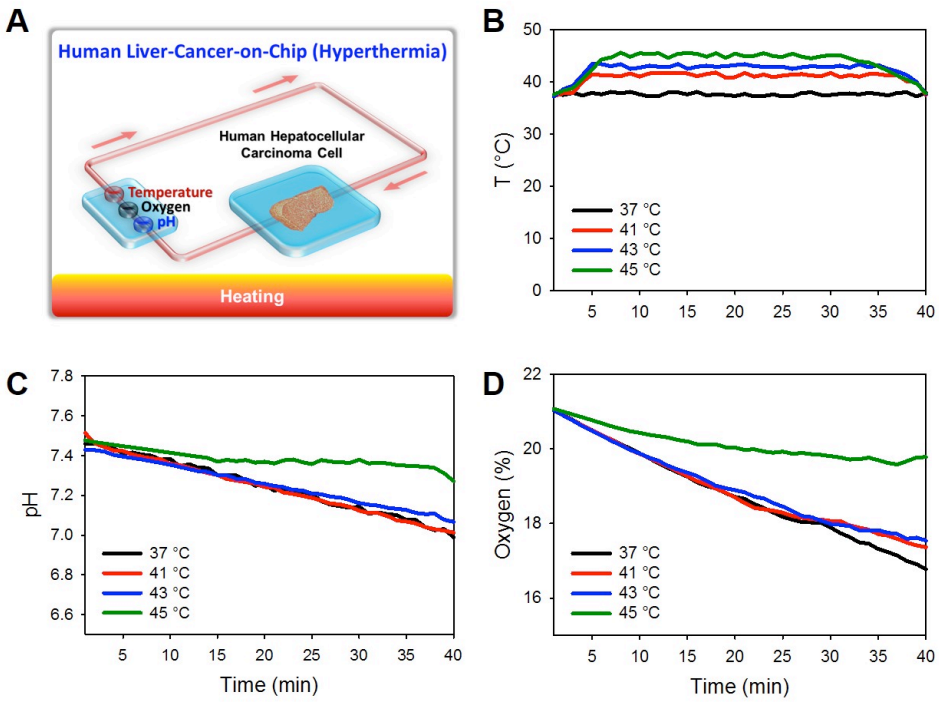

Fig. S31. Continuous monitoring of physical parameters of liver-cancer-on-chip system undergoing hyperthermia treatment. (**A**) Schematic showing the setup of the platform, where the temperatures of the environment were elevated to 41, 43, or 45 °C. (**B–D**) In-line measurements of temperatures, pH values, and oxygen levels, respectively.

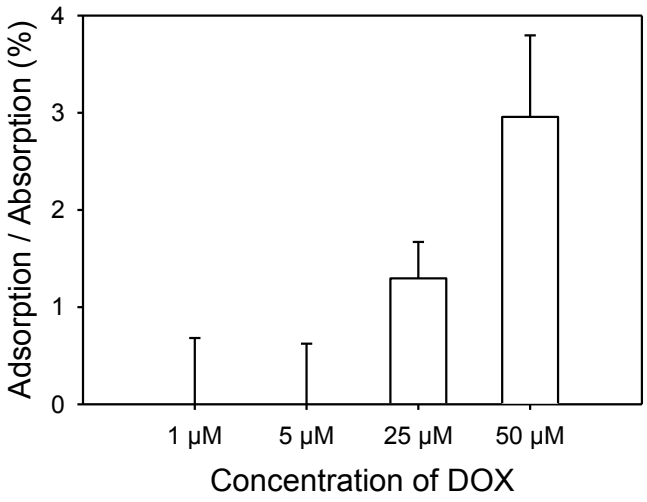

Fig. S32. Quantification of adsorption/absorption of DOX by the PDMS-based platform.